NANO LETTERS

Letter

pubs.acs.org/NanoLett

# Hole Selective $MoO_x$ Contact for Silicon Solar Cells

Corsin Battaglia,[†,‡,▽] Xingtian Yin,[†,‡,§,▽] Maxwell Zheng,[†,‡] Ian D. Sharp,[∥] Teresa Chen,[⊥] Stephen McDonnell,[○] Angelica Azcatl,[○] Carlo Carraro,[#] Biwu Ma,[⊥] Roya Maboudian,[#] Robert. M. Wallace,[○] and Ali Javey*[,†,‡]

[†]Electrical Engineering and Computer Sciences Department, University of California, Berkeley, California 94720, United States
[‡]Materials Sciences Division, Lawrence Berkeley National Laboratory, Berkeley, California 94720, United States
[§]Electronic Materials Research Laboratory, Xi'an Jiaotong University, Xi'an, 710049 Shaanxi, People's Republic of China
[∥]Joint Center for Artificial Photosynthesis, Lawrence Berkeley National Laboratory, Berkeley, California 94720, United States
[⊥]Molecular Foundry, Lawrence Berkeley National Laboratory, Berkeley, California 94720, United States
[○]Materials Science and Engineering, University of Texas, Dallas, Texas 75083, United States
[#]Chemical and Biomolecular Engineering, University of California, Berkeley, California 94720, United States

*S* *Supporting Information*

**ABSTRACT:** Using an ultrathin (~15 nm in thickness) molybdenum oxide ($MoO_x$, $x < 3$) layer as a transparent hole selective contact to n-type silicon, we demonstrate a room-temperature processed oxide/silicon solar cell with a power conversion efficiency of 14.3%. While $MoO_x$ is commonly considered to be a semiconductor with a band gap of 3.3 eV, from X-ray photoelectron spectroscopy we show that $MoO_x$ may be considered to behave as a high workfunction metal with a low density of states at the Fermi level originating from the tail of an oxygen vacancy derived defect band located inside the band gap. Specifically, in the absence of carbon contamination, we measure a work function potential of ~6.6 eV, which is significantly higher than that of all elemental metals. Our results on the archetypical semiconductor silicon demonstrate the use of nm-thick transition metal oxides as a simple and versatile pathway for *dopant-free* contacts to inorganic semiconductors. This work has important implications toward enabling a novel class of junctionless devices with applications for solar cells, light-emitting diodes, photodetectors, and transistors.

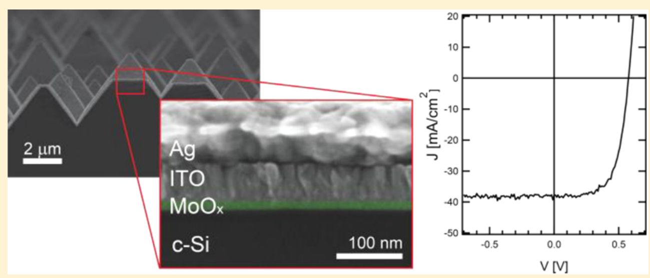


**KEYWORDS:** *Junctionless solar cells, silicon photovoltaics, heterojunctions, dopant-free contact, molybdenum trioxide*

Hybrid organic/inorganic solar cells combining an organic hole transport layer such as PEDOT:PSS, spiro-OMeTAD, or P3HT with n-type crystalline silicon have generated considerable interest as an alternative to traditional silicon photovoltaics with the potential to reduce cost by adopting room-temperature solution processing.[1−5] Power conversion efficiencies have been rising steadily over the past three years due to improvements of the organic hole transport materials, interface properties, and light management and have recently reached up to 13%.[2] However, further efficiency improvements are mandatory to render hybrid solar cells economically viable.

Hybrid organic/silicon devices now routinely achieve open-circuit voltages ($V_{oc}$) close to 600 mV, and focus has moved toward exploring various nanotexturing schemes, including metal-assisted chemical etching and reactive ion etching, to improve the short-circuit current density ($J_{sc}$).[1−3] However, nanotexturing often leads to difficulties with conformal coating of the organic hole contact.[2,4,5] In addition, the air and ultraviolet stability of polymers remains a major concern.[6,7]

Here we introduce a solar cell architecture using a transparent substoichiometric molybdenum trioxide ($MoO_x$, $x < 3$) with a sub-100 nm thickness as a hole-selective, dopant-free contact to n-type silicon. Transition metal oxides have been studied extensively as hole contacts for organic solar cells, organic light emitting diodes, and organic thin film transistors and have led to significant improvements in device performance and stability.[8−18] To our surprise, transition metal oxides have not yet been employed in conjunction with n-type silicon absorbers. In this work, we demonstrate a room-temperature processed $MoO_x$/silicon solar cell with a $V_{oc}$ of 580 mV implementing an industrially proven silicon pyramid texture for maximum light absorption reaching an efficiency of 14.3%. Using X-ray photoelectron spectroscopy (XPS), we further demonstrate that much of the controversy around the band alignment and electronic behavior of $MoO_x$[8,9] can be resolved by interpreting

**Received:** November 26, 2013
**Revised:** December 24, 2013
**Published:** January 7, 2014

   dx.doi.org/10.1021/nl404389u | *Nano Lett.* 2014, 14, 967−971

$MoO_x$ as a high workfunction metal with a low density of states at the Fermi level originating from a defect band inside the band gap.

$MoO_x$ thin films with a thickness of 40 nm were thermally evaporated onto flat n-type silicon (100) substrates with a carrier concentration of $10^{15}$ $cm^{-3}$ from stoichiometric $MoO_3$ powder at a rate of 0.5 Å/s from an $Al_2O_3$ coated W boat at a pressure in the mid $10^{-6}$ mbar range. The $Al_2O_3$ coating is important to guarantee a controlled evaporation rate. The substrates were etched in hydrofluoric acid right before loading into the evaporator. The electronic band structure was characterized via XPS using monochromated Al $K_\alpha$ X-rays with a photon energy of 1486.7 eV at a pressure in the low $10^{-9}$ to mid $10^{-10}$ mbar range. To study the valence band region and workfunction of $MoO_x$, Al $K_\alpha$ photons were chosen over the more conventional He I line with 21.2 eV radiation in order to benefit from the longer inelastic mean free path of photoelectrons resulting in increased probing depth (5−10 nm judging from the visibility of Si 2p photoelectrons from the silicon substrate) and consequently enhanced bulk sensitivity.

In order to correctly interpret the electronic structure of evaporated $MoO_x$ films it is important to understand their atomic structure. The $MoO_3$ single crystal structure is schematically shown in Figure 1a. Each Mo atom is surrounded by six octahedrally coordinated O atoms arranged into intertwined double layers which are stacked via van der Waals forces. One vertex of each octahedron extends into the van der Waal gaps, two vertices are shared with two neighboring octahedra, and the remaining three vertices are shared with three neighboring octahedra (octahedra joined by edges), resulting in an effective total of three O atoms per Mo atom.

Figure 1c and d show X-ray diffraction and Raman scattering data of a $MoO_3$ single crystal, grown by heating $MoO_3$ powder to 800 °C in a quartz tube furnace, while flowing $O_2$/Ar = 20%:80%, indicating sharp diffraction peaks and vibrational modes respectively. No such peaks are observed for the evaporated $MoO_x$ thin films, pointing toward an amorphous structure as shown in Figure 1b. An earlier X-ray absorption fine structure investigation[19] confirms that evaporated $MoO_x$ films retain the local octahedral coordination of the Mo cation, but confirms the absence of long-range order. In addition, octahedra in amorphous films are predominantly connected via vertices (not edges) to their six neighboring octahedra, resulting in a total of three O atoms per Mo cation.

We now focus on the implications of the amorphous structure on the valence or oxidation state of the Mo ions. The bottom curve in Figure 2a presents the photoelectron spectrum of the Mo 3*d* core level of the evaporated $MoO_x$ film. The core level is split into the $3d_{5/2}$ and $3d_{3/2}$ doublet centered at 232.8 and 236.0 eV, respectively, in good agreement with previous work.[20] We identify these two main components with the fully oxidized $Mo^{6+}$ valence state corresponding to an intact octahedral coordination consisting of six O atoms.

To obtain a satisfactory fit to the experimental XPS data, a second doublet at lower binding energy is required, which we

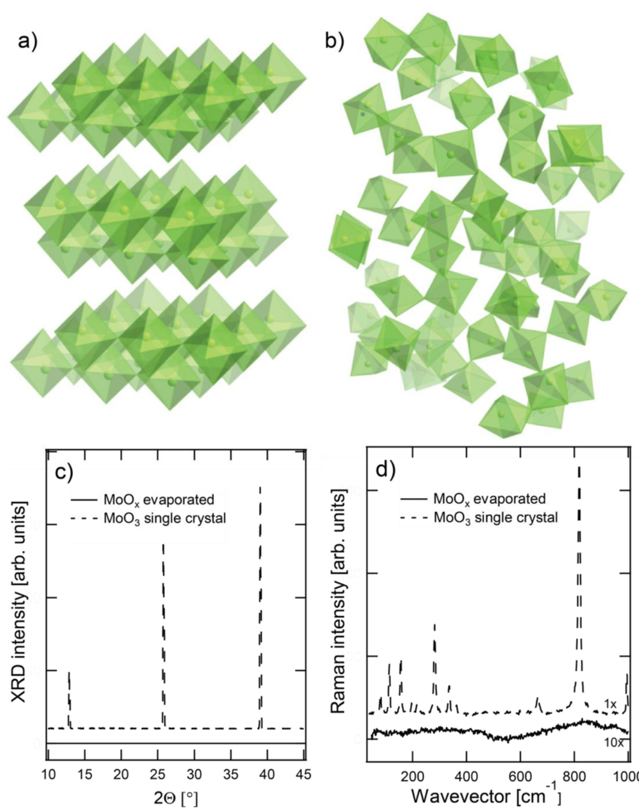


**Figure 1.** Sketch of the (a) crystalline and (b) amorphous atomic structure of $MoO_x$. (c) XRD and (d) Raman spectra. For Raman measurements $MoO_x$ was evaporated on a 100 nm thick sputtered Ag film on silicon. Elemental Ag shows no Raman signal as the face-centered cubic unit cell with only one atom supports acoustic phonons only, but no (Raman active) optical phonons.

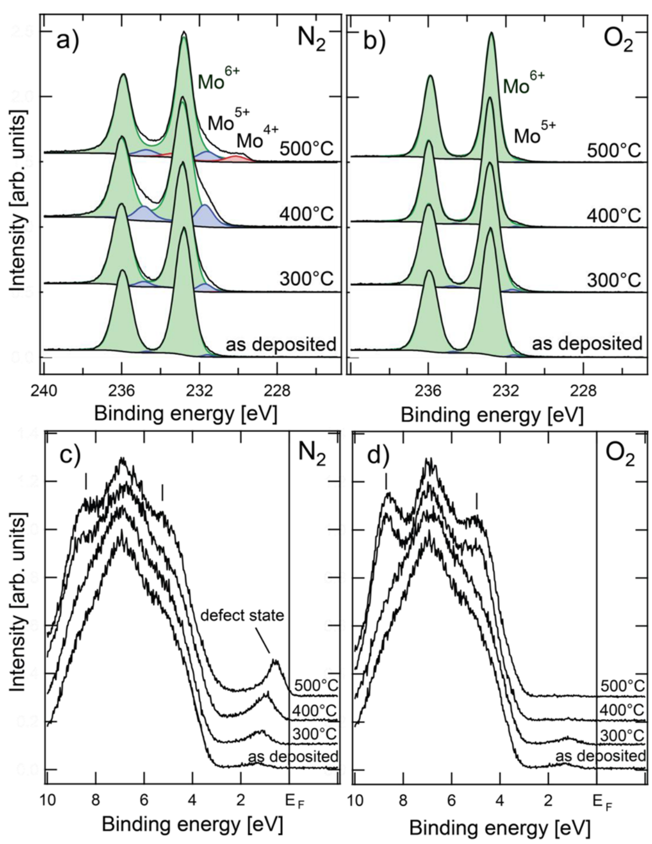


**Figure 2.** Effect of 30 s rapid thermal annealing in $N_2$ or $O_2$ ambient on the Mo 3*d* core level (a and b) and valence band region (c and d) of evaporated $MoO_x$ films. In (a) and (b) the individual fitted components are shown in color along with a Shirley background.

identify as the $Mo^{5+}$ valence state, corresponding to an oxygen vacancy at the vertex of an octahedron in the amorphous network. As the nearest neighbor correlation is preserved in the amorphous octahedron network, this reduced Mo state is expected to exhibit a relatively well-defined center energy smeared out to second order by the variations in local bond lengths and angles caused by the amorphous environment.

The valence state of the Mo cations can be reduced further by rapid thermal annealing in ambient $N_2$ as demonstrated in the stacked spectra in Figure 2a. With increasing annealing temperature the intensity of the $Mo^{5+}$ state increases significantly, which is consistent with the creation of additional oxygen vacancies. After annealing at 500 °C, we observe an additional shoulder in the Mo 3*d* core level at an even lower binding energy, which we identify as the $Mo^{4+}$ valence state corresponding to an octahedron with two missing O atoms. The formation of oxygen vacancies is reversible by annealing the amorphous $MoO_x$ network in ambient $O_2$ leading to a suppression of the $Mo^{5+}$ and $Mo^{4+}$ states as can be seen from Figure 2b. Annealing at high temperature leads to a partial crystallization of the $MoO_x$ films as witnessed by Raman spectroscopy (not shown), which can be avoided by reduction or oxidation at room temperature in atomic hydrogen or ozone environment respectively.

We now turn to the discussion of the valence band spectrum of the $MoO_x$ films shown in Figure 2c and d. The valence band spectra, which were also acquired using Al $K_\alpha$ photons, are dominated by the mostly O 2*p* derived bands extending from 3.2 eV to a higher binding energy. The edge of this O 2*p* derived band does not shift appreciably upon creation or annihilation of oxygen vacancies indicating that oxygen vacancies are not acting as shallow level donors in $MoO_x$. Of particular interest is the small defect band in the band gap visible in the as-deposited film at a binding energy of 1 eV. While this band has already been observed in early photoemission studies,[20] it has remained a source of controversy[8] concerning its implication on band alignment and charge transport in organic devices. Its spectral weight increases with increasing annealing temperature in $N_2$ (Figure 2c) and can be completely suppressed via annealing in ambient $O_2$ (Figure 2d).

Similar modifications of the valence band structure can be obtained through atomic hydrogen or ozone exposure avoiding the formation of the two shoulders in the O 2*p* valence band at binding energies of 5 and 9 eV (marked by the short vertical lines in Figure 2c and d) resulting from partial crystallization. These results are clear evidence that the defect band derives from the oxygen vacancies in the octahedron network; i.e. it is associated with Mo 4*d* electrons which remain loosely bound to the Mo atoms.

With increasing annealing temperature in $N_2$, we further observe a broadening and a shift of the center of the defect band toward the Fermi energy ($E_F$) at zero binding energy to a point where the band gap is completely filled up to the Fermi level. It is interesting to note that while fully stoichiometric $MoO_3$ with only $Mo^{6+}$ is insulating, $MoO_2$ with only $Mo^{4+}$ is known to be metallic and exhibits an unambiguous metallic Fermi-Dirac edge at zero binding energy.[20] As the detection limit for XPS is in the 1% atomic ratio range, we hypothesize that a small but finite density of states at the Fermi level below the detection limit of XPS is also present for the as-deposited $MoO_x$ film, even if the apparent defect density is much lower.

To strengthen our hypothesis, we compare in Figure 3a XPS valence spectra of evaporated $MoO_x$ before and after annealing at

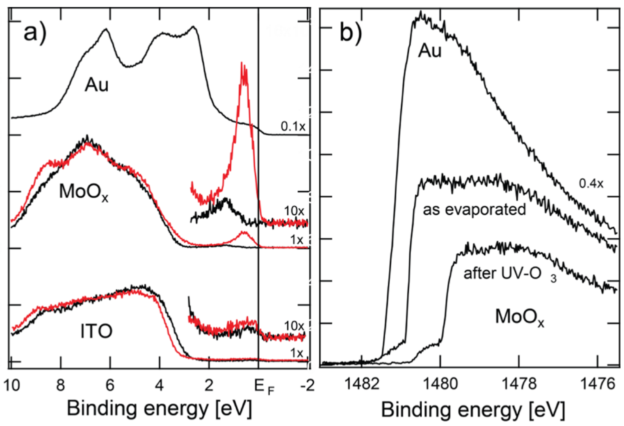


**Figure 3.** (a) Comparison of density of states at the Fermi level for ITO, $MoO_x$, and Au reference. The as-deposited $MoO_x$ film is shown in black, and the $N_2$ annealed film, in red. The ITO with $10^{21}$ and $10^{20}$ $cm^{-3}$ electrons are shown in red and black respectively. (b) Secondary electron cutoff for $MoO_x$ and Au reference. The intensity at the high binding energy side of the steep cutoff is due to an analyzer specific artifact. The evaporated $MoO_x$ film was exposed to UV-ozone (UV–$O_3$) to increase the workfunction by removal of adventitious carbon at the surface.

500 °C in $N_2$ with valence spectra of indium tin oxide (ITO) ($In_2O_3/SnO_2$ = 90%:10%). The ITO films were sputtered without and with oxygen in the argon plasma to tune the electron concentration to $10^{21}$ and $10^{20}$ $cm^{-3}$, respectively, as measured by the Hall effect. The region near the Fermi level for each spectrum is replotted with a scaling factor of 10 to allow easier comparison. The spectrum of a gold reference exhibiting a clear Fermi-Dirac step is also shown with a scaling factor of 0.1. While a metallic Fermi-Dirac edge of the ITO samples, already observed in ref 21 falls just within the detection limit of XPS, we do not observe any appreciable spectral weight at the Fermi level of the as-deposited $MoO_x$ films. Consequently we argue that spectral weight at the Fermi level corresponding to a Hall carrier density in the lower $10^{19}$ $cm^{-3}$ range or below cannot be detected by standard XPS. However, after annealing in $N_2$ at 500 °C, a significant density of states at the Fermi level of $MoO_x$ becomes apparent indicating metallic behavior, which we attribute to the appearance of $Mo^{4+}$ ions. Thus it is reasonable to assume that minute amounts of $Mo^{4+}$ ions are already present in the evaporated film and can cause metallic behavior.

For the ITO samples, the shift of the valence band maximum toward higher binding energy confirms that the Fermi level moves deeper into the conduction band with increasing carrier density. The creation of oxygen vacancies therefore dopes ITO with electrons. Interestingly such a shift is not observed for $MoO_x$ as a function of defect level intensity, indicating that the Fermi level does not move within the $MoO_3$ host when oxygen vacancies are created. Instead the band gap becomes filled with additional Mo 4*d* states.

Figure 3b shows secondary electron cut-offs of the photoelectron spectra, from which we extract the workfunction by extrapolating the linear part of the cutoff to zero intensity and subtracting this energy from the Al $K_\alpha$ X-ray excitation energy of 1486.7 eV (the spectra are corrected for an externally applied bias of −9.87 V on the sample, which accelerates photoelectrons away from the sample into the detector). The workfunction for the Au reference sputter cleaned in vacuo is 5.1 eV, in good agreement with values found in literature.[22] For the evaporated $MoO_x$ film transferred in air to the XPS chamber we obtain 5.7 eV. It is well-


dx.doi.org/10.1021/nl404389u | *Nano Lett.* 2014, 14, 967−971

known that the workfunction of $MoO_x$ is very sensitive to air exposure.[8] To explore the workfunction potential of evaporated $MoO_x$, we exposed the films to UV-ozone (UV−$O_3$) at 900 mbar for 30 min. From XPS, we see a reduction of adventitious carbon contamination (not shown)[23] and a dramatic increase of the workfunction to a value as high as 6.6 eV even with some residual C 1*s* signal. The same value was obtained after a prolonged 6 h exposure resulting in complete elimination of the C 1*s* signal below the detection limit. This clearly demonstrates the high workfunction and consequently electron affinity potential of $MoO_x$ exceeding those of elemental metals[24] and confirms earlier work on in situ evaporated $MoO_x$.[25] Even with slight carbon contamination, the workfunction remains sufficiently high to bring the Fermi level of $MoO_x$ close to the position of the valence band maximum of silicon located at 5.1 eV. $MoO_x$ can thus be used as a selective contact for a $MoO_x$/silicon solar cell.

Solar cells were fabricated by deposition of a 15 nm thick $MoO_x$ layer on a potassium hydroxide (KOH) textured silicon wafer right after removal of the native oxide in dilute hydrofluoric (HF) acid (see Figure 4a and b). After air exposure, the $MoO_x$ layer was covered with 55 nm of sputtered ITO deposited in an Ar plasma at $10^{-2}$ mbar and an evaporated 100 nm thick Ag grid with a finger width of 11 $\mu$m and pitch of 490 $\mu$m was patterned via photolithography and lift-off. We chose a hydrogenated amorphous silicon passivated ITO/Ag back contact capable of open-circuit voltages of up to 720 mV[26] in order to study the open-circuit voltage potential of the $MoO_x$/Si frontside heterojunction interface with minimum recombination at the backside. The finalized cells were annealed at 150 °C in $N_2$ for 10 min to improve the conductivity of the ITO electrode.[27]

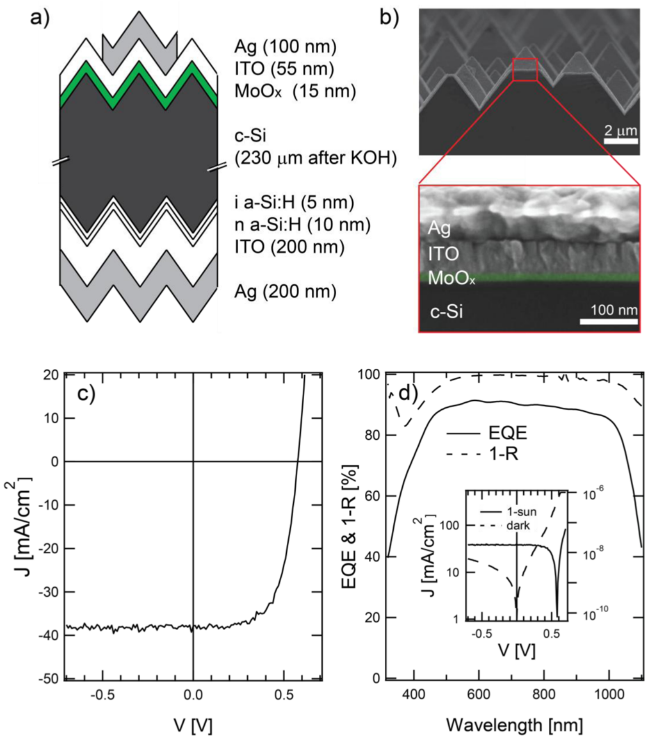


**Figure 4.** (a) Schematics of the $MoO_x$/n-Si heterojunction solar cell structure with (b) false-colored cross section imaged by scanning electron microscopy, (c) *J*−*V* and (d) EQE and 1 − *R* curve. The inset in (d) shows dark (right scale) and light (left scale) *J*−*V* curves in logarithmic scales. Pyramids in (a) are not drawn to scale and are not necessarily commensurate on front and back side.

Figure 4c presents the *J*−*V* curves for solar cells patterned and masked to an area of 5 mm × 5 mm and measured under standard test conditions (1000 W/m$^2$, air mass 1.5 global (AM1.5$_g$) spectrum and 25 °C). With an open-circuit voltage ($V_{oc}$) of 580 mV, a short-circuit current ($J_{sc}$) of 37.8 mA/cm$^2$ (including 2% grid shading) and a fill factor (FF) of 65%, a power conversion efficiency of 14.3% is obtained. The external quantum efficiency (EQE) and reflectance (*R*, presented as 1 − *R*, measured with an integrating sphere) are shown in Figure 4d along with the dark and light *J*−*V* curves in a semilogarithmic plot in the inset.

While our simple cell design with the unpassivated $MoO_x$/silicon interface cannot rival the performance of state-of-the-art silicon heterojunction solar cells, which integrate a sophisticated amorphous silicon passivation scheme,[18] it clearly illustrates the concept of a transparent dopant-free selective hole contact to n-type silicon. With a demonstrated $V_{oc}$ potential of 580 mV, our $MoO_x$/silicon solar cell nevertheless reaches values that are as high as those for the best-in-class hybrid organic/silicon solar cells (see Table S1). A significantly higher $J_{sc}$ is obtained due to the traditional pyramid texture in conjunction with a carefully optimized oxide layer thickness (see Supporting Information for more details) for minimum reflection losses which outperforms nanotextures obtained by metal-assisted etching or reactive ion etching. $MoO_x$/silicon consequently reaches an efficiency higher than that of hybrid organic/silicon solar cells.

Various potential improvements of our cell design can be envisioned including the implementation of a passivation layer with local $MoO_x$ contact openings or the addition of an intrinsic amorphous silicon passivation layer in conjunction with a $MoO_x$ contact to improve $V_{oc}$. The FF could be improved by optimizing the defect state density in the band gap of $MoO_x$ or by depositing an ultrathin highly conformal $MoO_x$ layer by atomic layer deposition. A higher $J_{sc}$ could be achieved by improving the ITO transparency and reducing shadowing due to the Ag finger grid. $MoO_x$ could also be replaced by other transition metal oxides such as $NiO_x$, $VO_x$, or $WO_x$, which have proven to function as hole contacts in organic electronics.[8] Furthermore $MoO_x$ along with ITO and other transparent conductive oxides were shown to be compatible with solution processing[11,13,27] enabling a route toward a low-cost, fully solution-processed cell architecture.

In conclusion, we demonstrated a simple $MoO_x$/silicon solar cell with an efficiency of 14.3%. With a high workfunction exceeding those of elemental metals, $MoO_x$ presents an important opportunity for hole contact in not only inorganic semiconductor materials with low lying valence band maxima including III−V semiconductors such as InP or GaN but also layered transition metal dichalcogenide semiconductors as well as oxide- and carbon-based nanomaterials.

## ■ ASSOCIATED CONTENT

### Supporting Information

Compilation of hybrid organic/silicon solar cell performance characteristics. Optimization of ITO/$MoO_x$ thicknesses. This material is available free of charge via the Internet at http://pubs.acs.org.

## ■ AUTHOR INFORMATION

### Corresponding Author

*E-mail: ajavey@eecs.berkeley.edu.

### Author Contributions

▽Authors with equal contribution.

### Notes

The authors declare no competing financial interest.

## ■ ACKNOWLEDGMENTS

$MoO_x$ processing and characterization were funded by the Center for Low Energy Systems Technology (LEAST), one of the six SRC STARnet centers sponsored by MARCO and DARPA. Photovoltaic device fabrication and characterization were funded by the Bay Area Photovoltaics Consortium (BAPVC). Some of the XPS measurements were performed at JCAP; this material is based upon work performed by the Joint Center for Artificial Photosynthesis, a DOE Energy Innovation Hub, supported through the Office of Science of the U.S. Department of Energy under Award Number DE-SC0004993. We thank L. Barraud, S. De Wolf, and C. Ballif from the Ecole Polytechnique Federale de Lausanne (EPFL) for providing textured silicon wafers with passivated back contacts. C.B. acknowledges support from the Zeno Karl Schindler Foundation. A.J. acknowledges support from the BK21 Plus program at Sunchon National University.

## ■ REFERENCES

(1) See Table S1 for a compilation of device performance characteristics

(2) Yu, P.; Tsai, C.-Y.; Chang, J.-K.; Lai, C.-C.; Chen, P.-H.; Lai, Y.-C.; Tsai, P.-T.; Li, M.-C.; Pan, H.-T.; Huang, Y.-Y.; Wu, C.-I.; Chueh, Y.-L.; Chen, S.-W.; Du, C.-H.; Horng, S.-F.; Meng, H.-F. 13% Efficiency Hybrid Organic/Silicon-Nanowire Heterojunction Solar Cell via Interface Engineering. *ACS Nano* **2013**, *7*, 10780.

(3) Jeong, S.; Garnett, E. C.; Wang, S.; Yu, Z.; Fan, S.; Brongersma, M. L.; McGehee, M. D.; Cui, Y. Hybrid Silicon Nanocone-polymer Solar Cells. *Nano Lett.* **2012**, *12*, 2971.

(4) He, L.; Jiang, C.; Rusli; Lai, D.; Wang, H. Highly efficient Si-nanorods/organic hybrid core-sheath heterojunction solar cells. *Appl. Phys. Lett.* **2011**, *99*, 021104.

(5) Chen, T. G.; Huang, B. Y.; Chen, E. C.; Yu, P. C.; Meng, H. F. Micro-textured conductive polymer/silicon heterojunction photovoltaic devices with high efficiency. *Appl. Phys. Lett.* **2012**, *101*, 033301.

(6) Jorgensen, M.; Norman, K.; Krebs, F. C. Stability/degradation of polymer solar cells. *Sol. Energy Mater. Sol. Cells* **2008**, *92*, 686−714.

(7) Reese, M. O.; Gevorgyan, S. A.; Jorgensen, M.; Bundgaard, E.; Kurtz, S. R.; et al. Consensus stability testing protocols for organic photovoltaic materials and devices. *Sol. Energy Mater. Sol. Cells* **2011**, *95*, 1253−1267.

(8) Meyer, J.; Hamwi, S.; Kröger, M.; Kowalsky, W.; Riedl, T.; Kahn, A. Transition Metal Oxides for Organic Electronics: Energetics, Device Physics and Applications. *Adv. Mater.* **2012**, *24*, 5408−5427.

(9) Greiner, M. T.; Helander, M. G.; Tang, W.-M.; Wang, Z.-B.; Qiu, J.; Lu, Z.-H. Universal energy-level alignment of molecules on metal oxides. *Nat. Mater.* **2012**, *11*, 76.

(10) Papadopoulos T. A.; Meyer J.; Li H.; Guan Z.; Kahn A.; Brédas J.-L. Nature of the Interfaces Between Stoichiometric and Under-Stoichiometric $MoO_3$ and 4,4-N,N′-dicarbazole-biphenyl: A Combined Theoretical and Experimental Study, *Adv. Funct. Mater.*, early online view DOI: 10.1002/adfm.201301466.

(11) Murase, S.; Yang, Y. Solution Processed $MoO_3$ Interfacial Layer for Organic Photovoltaics Prepared by a Facile Synthesis Method. *Adv. Mater.* **2012**, *24*, 2459.

(12) Sun, Y.; Takacs, C. J.; Cowan, S. R.; Seo, J. W.; Gong, X.; Roy, A.; Heeger, A. J. Efficient, Air-Stable Bulk Heterojunction Polymer Solar Cells Using $MoO_x$ as the Anode Interfacial Layer. *Adv. Mater.* **2011**, *23*, 2226−2230.

(13) Stubhan, T.; Ameri, T.; Salinas, M.; Krantz, J.; Machui, F.; Halik, M.; Brabec, C. J. High shunt resistance in polymer solar cells comprising a $MoO_3$ hole extraction layer processed from nanoparticle suspension. *Appl. Phys. Lett.* **2011**, *98*, 253308.

(14) Kröger, M.; Hamwi, S.; Meyer, J.; Riedl, T.; Kowalsky, W.; Kahn, A. Role of deep-lying electronic states of $MoO_3$ in the enhancement of hole-injection in organic thin films. *Appl. Phys. Lett.* **2009**, *95*, 123301.

(15) Lee, H.; Cho, S. W.; Han, K.; Jeon, P. E.; Whang, C.-M.; Jeong, K.; Cho, K.; Yi, Y. The origin of hole injection improvements at the indium tin oxide/molybdenum trioxide/N,N′-bis(1-naphthyl)-N,N′-diphenyl-1,1′-biphenyl-4,4′-diamine interfaces. *Appl. Phys. Lett.* **2008**, *93*, 043308.

(16) Kanno, H.; Holmes, R. J.; Sun, Y.; Kena-Cohen, S.; Forrest, S. R. White Stacked Electrophosporescent Organic Light-Emitting Devices Employing $MoO_3$ as a Charge-Generation Layer. *Adv. Mater.* **2006**, *18*, 339.

(17) Chu, C.-W.; Li, S.-H.; Chen, C.-W.; Shrotriya, V.; Yang, Y. High-performance organic thin-film transistors with metal oxide/metal bilayer electrode. *Appl. Phys. Lett.* **2005**, *87*, 193508.

(18) Tokito, S.; Noda, K.; Taga, Y. Metal oxides as hole-injection layer for an organic electroluminescent device. *J. Phys. D: Appl. Phys.* **1996**, *29*, 2750−2753.

(19) Burattini, E. XAFS Studies of Octahedral Amorphous Oxides. *Jpn. J. Appl. Phys.* **1993**, *32*, 655−657.

(20) Werfel, F.; Minni, E. Photoemission study of the electronic structure of Mo and Mo oxides. *J. Phys. C: Solid State Phys.* **1983**, *16*, 6091−6100.

(21) Walsh, A.; Da Silva, J. L. F.; Wei, S.-H.; Körber, C.; Klein, A.; Piper, L. F. J.; DeMasi, A.; Smith, K. E.; Panaccione, G.; Torelli, P.; Payne, D. J.; Bourlange, A.; Egdell, R. G. Nature of the band gap in $In_2O_3$ by first-principles calculations and X-ray spectroscopy. *Phys. Rev. Lett.* **2008**, *100*, 167402.

(22) Baer, Y. The natural energy scale for XPS spectra of metals. *Sol. State. Comm.* **1976**, *19*, 669−671.

(23) Barr, T. L.; Seal, S. Nature of the use of adventitious carbon as binding energy standard. *J. Vac. Sci. Technol. A* **1995**, *13*, 1239.

(24) Michaelson, H. B. The work function of the elements and its periodicity. *J. Appl. Phys.* **1977**, *48*, 4729.

(25) Meyer, J.; Shu, A.; Kröger, M.; Kahn, A. Effect of contamination on the electronic structure and hole-injection properties of $MoO_3$/organic semiconductor interfaces. *App. Phys. Lett.* **2010**, *96*, 133308.

(26) Barraud, L.; Holman, Z. C.; Badel, N.; Reiss, P.; Descoeudres, A.; Battaglia, C.; De Wolf, S.; Ballif, C. Hydrogen-doped indium oxide/indium tin oxide bilayers for high-efficiency silicon heterojunction solar cells. *Sol. Energy Mater. Sol. Cells* **2013**, *115*, 151−156.

(27) Battaglia, C.; Erni, L.; Boccard, M.; Barraud, L.; Escarré, J.; Söderström, K.; Bugnon, G.; Billet, A.; Ding, L.; Despeisse, M.; Haug, F.-J.; De Wolf, S.; Ballif, C. Micromorph thin-film silicon solar cells with transparent high-mobility hydrogenated indium oxide front electrodes. *J. Appl. Phys.* **2011**, *109*, 114501.

(28) Pasquarelli, R. M.; Ginley, D. S.; O'Hayre, R. Solution processing of transparent conductors: from flask to film. *Chem. Soc. Rev.* **2011**, *40*, 5406−5441.

# Hole selective $MoO_x$ contact for silicon solar cells

Corsin Battaglia[1,2,#], Xingtian Yin[1,2,3,#], Maxwell Zheng[1,2], Ian D. Sharp[4], Teresa Chen[5], Stephen McDonnell[6], Angelica Azcatl[6], Carlo Carraro[7], Roya Maboudian[7], Robert. M. Wallace[6] and Ali Javey[1,2,*]

[1]*Electrical Engineering and Computer Sciences Department, University of California, Berkeley, CA 94720*

[2]*Materials Sciences Division, Lawrence Berkeley National Laboratory, Berkeley, CA 94720*

[3]*Electronic Materials Research Laboratory, Xi'an Jiaotong University, Xi'an, 710049 Shaanxi, People's Republic of China*

[4]*Joint Center for Artificial Photosynthesis, Lawrence Berkeley National Laboratory, Berkeley, CA 94720*

[5]*Molecular Foundry, Lawrence Berkeley National Laboratory, Berkeley, CA 94720*

[6]*Materials Science and Engineering, University of Texas, Dallas, TX 75083*

[7]*Chemical and Biomolecular Engineering, University of California, Berkeley, CA 94720*

[#]Authors with equal contribution

*Corresponding Author: ajavey@eecs.berkeley.edu

# Supporting information

**Table S1:** Compilation of hybrid organic/silicon solar cell performance characteristics, also included are results for graphene/silicon and carbon nanotubes/silicon solar cells.

| **Reference** | **Hole contact** | **Texture** | **$V_{oc}$ [mV]** | **$J_{sc}$ [mA/cm$^2$]** | **FF [%]** | **Efficiency [%]** |
|---|---|---|---|---|---|---|
| This work | $MoO_x$/ITO | KOH | 580 | 37.8 | 65.0 | 14.3 |
| Yu et al., ACS Nano, 2013 [1] | TAPC/PEDOT:PSS | $AgNO_3$+HF | 540 | 34.8 | 69.5 | 13.0 |
| Nagamatsu et al., IEEE JPV 2013 [2] | PEDOT :PSS | None | 570 | 27.8 | 73.0 | 11.7 |
| Wei et al., Nano Lett., 2013 [3] | PEDOT:PSS | KOH/Au +$H_2O_2$+HF | 520 | 34.5 | 64.1 | 11.5 |
| Liu et al., Appl. Phys. Lett., 2012 [4] | PEDOT:PSS | None | 541 | 29.2 | 71.8 | 11.3 |
| Jung et al., Nano Lett., 2012 [5] | Carbon nanotubes | None | 530 | 28.6 | 74.1 | 11.2 |
| Jeong et al., Nano Lett. 2012 [6] | PEDOT:PSS | RIE | 550 | 29.6 | 67.7 | 11.1 |
| Ono et al., Appl. Phys. Exp., 2012 [7] | Graphene/PEDOT:PSS | none | 548 | 28.9 | 67.5 | 10.7 |
| He et al., Appl. Phys. Lett., 2012 [8] | PEDOT:PSS | none | 610 | 26.4 | 65.9 | 10.6 |
| He, Appl. Phys. Lett., 2011 [9] | Spiro-OMeTAD/PEDOT:PSS | $AgNO_3$+HF | 570 | 30.9 | 58.8 | 10.3 |
| Zhang et al., J. Mat. Chem. A, 2013 [10] | Graphene | $AgNO_3$+HF | 552 | 38.86 | 48.0 | 10.3 |
| Avasthi et al., Adv. Mat., 2011 [11] | P3HT/PEDOT:PSS | None | 590 | 29 | 59.0 | 10.1 |
| He et al., ACS Appl. Mater. Inter., 2012 [12] | Spiro-OMeTAD/PEDOT:PSS | $AgNO_3$+HF | 570 | 30.7 | 56.6 | 9.9 |
| Zhu et al., Appl. Phys. Lett., 2013 [13] | PEDOT:PSS/PFI | None | 560 | 25.3 | 70.0 | 9.9 |
| Chen et al., Appl. Phys. Lett., 2012 [14] | PEDOT:PSS | KOH | 520 | 30.4 | 62.1 | 9.8 |

| | | | | | | |
|---|---|---|---|---|---|---|
| Shen et al., JACS, 2011 [15] | Spiro-OMeTAD/PEDOT:PSS | $AgNO_3$+HF | 527 | 31.3 | 58.8 | 9.7 |
| Zhang et al., J. Mat. Chem., 2012 [16] | P3HT/PEDOT:PSS | $AgNO_3$+HF | 457 | 37.6 | 54 | 9.2 |
| He et al., IEEE Electron Device Lett., 2011 [17] | PEDOT:PSS | $AgNO_3$+HF | 530 | 26.3 | 64.2 | 9.0 |
| Zhang et al., Appl. Phys. Lett., 2013 [18] | PEDOT:PSS | $AgNO_3$+HF | 500 | 29.8 | 58 | 8.7 |
| Syu et al., Sol. Energy Mat. & Sol. Cells, 2012 [19] | PEDOT:PSS | $AgNO_3$+HF | 532 | 24.2 | 65.1 | 8.4 |
| Zhang et al., Nanotechnology 2012 [20] | PEDOT:PSS | $AgNO_3$+HF | 497 | 30.7 | 48 | 7.3 |
| Lu et al., Nanoscale, 2011 [21] | PEDOT:PSS | $AgNO_3$+HF | 460 | 21.6 | 64 | 6.4 |
| Cui et al., J. Mat. Chem. A, 2013 [22] | Graphene | none | 548 | 17.9 | 60.6 | 6.0 |
| Zhang et al., Chem. Mat. 2013 [23] | P3HT/PEDOT:PSS | $AgNO_3$+HF | 421 | 26.2 | 53 | 5.9 |
| He et al., Appl. Phys. Lett., 2012 [24] | PEDOT:PSS | $AgNO_3$+HF | 570 | 13.6 | 71.9 | 5.6 |
| Feng et al., Nanoscale 2012 [25] | Graphene/ $HNO_3$ | ICP | 495 | 17.22 | 51 | 4.4 |
| Liu et al., Nanoscale Res. Lett., 2013 [26] | PEDOT:PSPS | $AgNO_3$+HF | 455 | 16.6 | 42.9 | 3.2 |
| Tsai et al., ACS Nano, 2011, [27] | P3HT | $AgNO_3$+HF | 346 | 18.9 | 35.2 | 2.3 |
| Li et al., Adv Mater., 2010 [28] | Graphene | none | 420~480 | 4~6.5 | 45~56 | 1~1.7 |

## Optimization of $MoO_x$/ITO thicknesses

The front reflectance of a cell with a double layer antireflection coating is giving by the following expression [29]:

$R=A/B$

where

$A= r_1^2+r_2^2+r_3^2+r_1^2\cdot r_2^2\cdot r_3^2+2r_1\cdot r_2(1+r_3^2) \cdot\cos(2\cdot\theta_1)+2\cdot r_2\cdot r_3\cdot (1+r_1^2) \cdot\cos(2\cdot\theta_2)+2\cdot r_1\cdot r_3\cdot\cos[2\cdot (\theta_1+\theta_2)]+2\cdot r_1\cdot r_2^2\cdot r_3\cdot\cos[2\cdot (\theta_1-\theta_2)]$

$B=1+r_1^2\cdot r_2^2+r_1^2\cdot r_3^2+r_2^2\cdot r_3^2+2\cdot r_1\cdot r_2\cdot (1+r_3^2) \cdot\cos(2\cdot\theta_1)+2\cdot r_2\cdot r_3(1+r_1^2) \cdot\cos(2\cdot\theta_2)+2\cdot r_1\cdot r_3\cdot\cos[2\cdot (\theta_1+\theta_2)]+2\cdot r_1\cdot r_2^2\cdot r_3\cdot\cos[2\cdot (\theta_1-\theta_2)]$

with

$r_1=(n_0-n_1)/(n_0+n_1)$

$r_2=(n_1-n_2)/(n_1+n_2)$

$r_3=(n_2-n_3)/(n_2+n_3)$

$\theta_1=(2\cdot\pi\cdot n_1\cdot t_1/\lambda)$

$\theta_2=(2\cdot\pi\cdot n_2\cdot t_2/\lambda)$

$n_1$, $n_2$, $n_3$ are the refractive indices of ITO, $MoO_x$ and Si in our case, $t_1$ and $t_2$ the ITO and $MoO_x$ thicknesses and $\lambda$ the wavelength. The refractive indices of ITO and $MoO_x$ are almost identical, so that we can assume that $r_2\approx 0$. In this case, A and B simplify to

$A= r_1^2 +r_3^2+2\cdot r_1\cdot r_3\cdot\cos[2\cdot (\theta_1+\theta_2)]$

$B=1 +r_1^2\cdot r_3^2+2\cdot r_1\cdot r_3\cdot\cos[2\cdot (\theta_1+\theta_2)]$

From R, we can determine the absorbance A=1-R. Convolution of A with the global air mass 1.5 spectrum and integration over all wavelength $\lambda$, gives an estimation of the maximum achievable short-circuit current density ($J_{sc}$) assuming no parasitic light absorption, unity carrier collection and total light trapping. Estimated $J_{sc}$ values as a function of the thicknesses of ITO and $MoO_x$ are shown in Fig. S1.

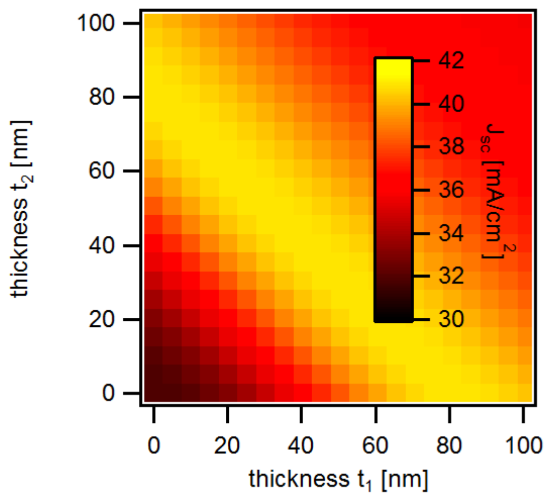


FIG. S1. Estimated $J_{sc}$ values for a flat silicon cell with ITO ($t_1$) and $MoO_x$ ($t_2$) layers.

For the pyramidal texture shown in Fig. 4a, most incoming light rays, which are reflected off a first time at a pyramid, hit subsequently a neighboring pyramid and undergo a second reflection event. Thus the effective reflectance of a pyramidally textured surface is given to a first approximation by $R_{pyramid}=R_{flat}^2$ [30, 31]. This renders the $J_{sc}$ much more tolerant to variations in layer thicknesses.

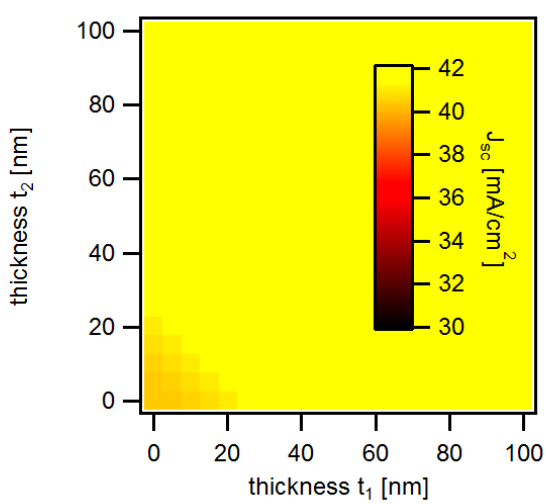


FIG. S2. Estimated $J_{sc}$ values for a pyramidally textured silicon cell with ITO ($t_1$) and $MoO_x$ ($t_2$) layers.

Due to the increased surface area of the pyramids compared to the flat surface, the evaporated/sputtered thicknesses of the antireflection layer on the pyramids must be scaled by a factor 1/cos(54.7°)≈1.7 compared to the flat surface in order to obtain the same effective thickness on the pyramids.

In practice, it is best to optimize the ITO and $MoO_x$ thicknesses directly on flat silicon. Ideally a dark blue color is observed typically at a total oxide thickness of 65 nm to 70 nm (see Fig. S3). The thicknesses are then scaled with a factor of 1.7 and transferred to the pyramid structure.

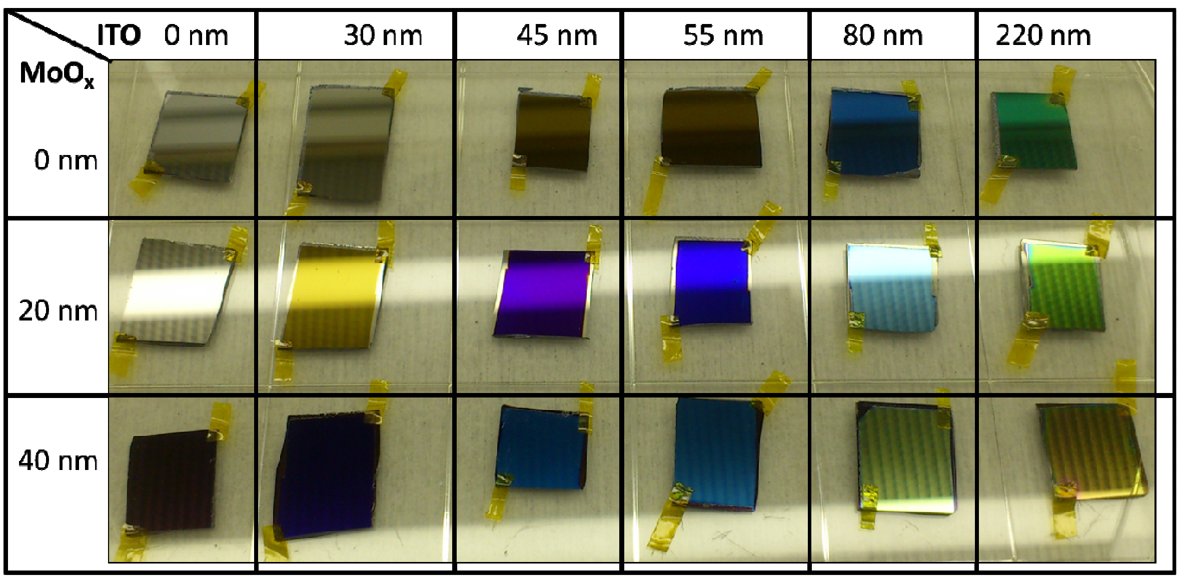


FIG. S3 Optimization of ITO and $MoO_x$ thicknesses on silicon wafer. An ideal dark blue color is observed at 65-70 nm total oxide thickness.

**References**

[1]. Yu, P.; Tsai, C.-Y.; Chang, J.-K.; Lai, C.-C.; Chen, P.-H.; Lai, Y.-C.; Tsai, P.-T.; Li, M.-C.; Pan, H.-T.; Huang, Y.-Y.; Wu, C.-I.; Chueh, Y.-L.; Chen, S.-W.; Du, C.-H.; Horng, S.-F.; Meng, H.-F., 13% Efficiency Hybrid Organic/Silicon-Nanowire Heterojunction Solar Cell via Interface Engineering, *ACS Nano* **2013**, 7, 10780.

[2]. Nagamatsu K. A.; Avasthi S.; Jhaveri J.; Sturm J. C., A 12% Efficient Silicon/PEDOT:PSS Heterojunction Solar Cell Fabricated at < 100° C, *IEEE J. Photovolt.*, **2013**, 4, 260

[3]. Wei, W.-R.; Tsai, M.-L.; Ho, S.-T.; Tai, S.-H.; Ho, C.-R.; Tsai, S.-H.; Liu, C.-W.; Chung, R.-J.; He, J.-H., Above-11%-Efficiency Organic-inorganic Hybrid Solar Cells with Omnidirectional Harvesting Characteristics by Employing Hierarchical Photon-Trapping Structures, *Nano Lett.* **2013**, 13, 3658.

[4]. Liu, Q.; Ono, M.; Tang, Z.; Ishikawa, R.; Ueno, K.; Shirai, H., Highly efficient crystalline silicon/Zonyl fluorosurfactant-treated organic heterojunction solar cells, *Appl. Phys. Lett.* **2012**, 100, 183901.

[5]. Jung, Y.; Li, X.; Rajan, N. K.; Taylor, A. D.; Reed, M. A., Record High Efficiency Single-Walled Carbon Nanotube/Silicon p-n Junction Solar Cells, *Nano Lett.* **2013**, 13, 95.

[6]. Jeong, S.; Garnett, E. C.; Wang, S.; Yu, Z.; Fan, S.; Brongersma, M. L.; McGehee, M. D.; Cui, Y., Hybrid Silicon Nanocone-polymer Solar Cells, *Nano Lett.* **2012**, 12, 2971.

[7]. Ono, M.; Tang, Z.; Ishikawa, R.; Gotou, T.; Ueno, K.; Shirai, H., Efficient Crystalline Si/Poly(ethylene dioxythiophene): Poly(styrene sulfonate): Graphene Oxide Composite Heterojunction Solar Cells, *Appl. Phys. Express* **2012**, 5, 032301.

[8]. He, L.; Jiang, C.; Wang, H.; Lai, D.; Rusli, High efficiency planar Si/organic heterojunction hybrid solar cells, *Appl. Phys. Lett.* **2012**, 100, 073503.

[9]. He, L.; Jiang, C.; Rusli; Lai, D.; Wang, H., Highly efficient Si-nanorods/organic hybrid core-sheath heterojunction solar cells, *Appl. Phys. Lett.* **2011**, 99, 021104.

[10]. Zhang, X.; Xie, C.; Jie, J.; Zhang, X.; Wu, Y.; Zhang, W., High-efficiency graphene/Si nanoarray Schottky junction solar cells via surface modification and graphene doping, *J. Mater. Chem. A* **2013**, 1, 6593.

[11]. Avasthi, S.; Lee, S.; Loo, Y.-L.; Sturm, J. C., Role of Majority and Minority Carrier Barriers Silicon/Organic Hybrid Heterojunction Solar Cells, *Adv. Mater.* **2011**, 23, 5762.

[12]. He, L.; Jiang, C.; Wang, H.; Lai, D.; Rusli, Si Nanowires Organic Semiconductor Hybrid Heterojunction Solar Cells Toward 10% Efficiency, *ACS Appl. Mater. Interfaces* **2012**, 4, 1704.

[13]. Zhu, Y.; Song, T.; Zhang, F.; Lee, S.-T.; Sun, B., Efficient organic-inorganic hybrid Schottky solar cell: The role of built-in potential, *Appl. Phys. Lett.* **2013**, 102, 113504.

[14]. Chen, T. G.; Huang, B. Y.; Chen, E. C.; Yu, P. C.; Meng, H. F., Micro-textured conductive polymer/silicon heterojunction photovoltaic devices with high efficiency, *Appl. Phys. Lett.* **2012**, 101, 033301.

[15]. Shen, X.; Sun, B.; Liu, D.; Lee, S.-T., Hybrid Heterojunction Solar Cell Based on Organic-inorganic Silicon Nanowire Array Architecture, *J. Am. Chem. Soc.* **2011**, 133, 19408.

[16]. Zhang, F.; Han, X.; Lee, S.-t.; Sun, B., Heterojunction with organic thin layer for three dimensional high performance hybrid solar cells, *J. Mater. Chem.* **2012**, 22, 5362.

[17]. Lining, H.; Rusli; Changyun, J.; Hao, W.; Lai, D., Simple Approach of Fabricating High Efficiency Si Nanowire/Conductive Polymer Hybrid Solar Cells, *IEEE Electron Device Lett.* **2011**, 32, 1406.

[18]. Zhang, J.; Zhang, Y. F.; Zhang, F. T.; Sun, B. Q., Electrical characterization of inorganic-organic hybrid photovoltaic devices based on silicon-poly(3,4-ethylenedioxythiophene):poly(styrenesulfonate), *Appl. Phys. Lett.* **2013**, 102, 013501.

[19]. Syu, H.-J.; Shiu, S.-C.; Lin, C.-F., Silicon nanowire/organic hybrid solar cell with efficiency of 8.40%, *Sol. Energy Mater. Sol. Cells* **2012**, 98, 267-272.

[20]. Zhang, F.; Song, T.; Sun, B., Conjugated polymer-silicon nanowire array hybrid Schottky diode for solar cell application, *Nanotechnology* **2012**, 23, 194006.

[21]. Lu, W.; Wang, C.; Yue, W.; Chen, L., Si/PEDOT:PSS core/shell nanowire arrays for efficient hybrid solar cells, *Nanoscale* **2011**, 3, 3631.

[22]. Cui, T.; Lv, R.; Huang, Z.-H.; Chen, S.; Zhang, Z.; Gan, X.; Jia, Y.; Li, X.; Wang, K.; Wu, D.; Kang, F., Enhanced efficiency of graphene/silicon heterojunction solar cells by molecular doping, *J. Mater. Chem. A* **2013**, 1, 5736.

[23]. Zhang, F.; Sun, B.; Song, T.; Zhu, X.; Lee, S., Air Stable, Efficient Hybrid Photovoltaic Devices Based on Poly(3-hexylthiophene) and Silicon Nanostructures, *Chem. Mater.* **2013**, 23, 2084.

[24]. He, L.; Jiang, C.; Wang, H.; Lai, D.; Heng Tan, Y.; Seng Tan, C.; Rusli, Effects of nanowire texturing on the performance of Si/organic hybrid solar cells fabricated with a 2.2 um thin-film Si absorber, *Appl. Phys. Lett.* **2012**, 100, 103104.

[25]. Feng, T.; Xie, D.; Lin, Y.; Zhao, H.; Chen, Y.; Tian, H.; Ren, T.; Li, X.; Li, Z.; Wang, K.; Wu, D.; Zhu, H., Efficiency enhancement of graphene/silicon-pillar-array solar cells by HNO3 and PEDOT-PSS, *Nanoscale* **2012**, 4, 2130.

[26]. Liu, K.; Qu, S.; Zhang, X.; Tan, F.; Wang, Z., Improved photovoltaic performance of silicon nanowire/organic hybrid solar cells by incorporating silver nanoparticles, *Nanoscale Res. Lett.* **2013**, 8, 88.

[27]. Tsai, S.-H.; Chang, H.-C.; Wang, H.-H.; Chen, S.-Y.; Lin, C.-A.; Chen, S.-A.; Chueh, Y.-L.; He, J.-H., Significant Efficiency Enhancement of Hybrid Solar Cells Using Core-shell Nanowire Geometry for Energy Harvesting, *ACS Nano* **2011**, 5, 9501.

[28]. Li, X.; Zhu, H.; Wang, K.; Cao, A.; Wei, J.; Li, C.; Jia, Y.; Li, Z.; Li, X.; Wu, D., Graphene-On-Silicon Schottky Junction Solar Cells, *Adv. Mater.* **2010**, 22, 2743.

[29] Wang E. Y.; Yu F. T. S.; Sims V. L.; Brandhorst E. W.; Broder J. D., Optimum design of anti-reflection coating for silicon solar cells, *Proc. of the 10$^{th}$ IEEE PVSC* **1973**, 168.

[30] Campbell P.; Green M. A., Light trapping properties of pyramidally textured surfaces, *J. Appl. Phys.* **1987**, 62, 243.

[31] Escarré J.; Soederstroem K.; Despeisse M.; Nicolay S.; Battaglia C.; Bugnon G.; Ding L.; Meillaud F.; Haug F.-J.; Ballif C., Geometric light trapping for high efficiency thin film silicon solar cells, *Sol. Ene. Mater. Sol. Cells* **2012**, 98, 185